A new site: ground-based FTIR XCO$_2$, XCH$_4$ and XCO measurements at Xianghe, China

Yang Yang[1,3,2], Minqiang Zhou[2], Bavo Langerock[2], Mahesh Kumar Sha[2], Christian Hermans[2], Ting Wang[1,3], Denghui Ji[1,3], Corinne Vigouroux[2], Nicolas Kumps[2], Gengchen Wang[1,3], Martine De Mazière[2], and Pucai Wang[1,3]

[1]LAGEO, the Institute of Atmospheric Physics, Chinese Academy of Sciences, Beijing, China
[2]Royal Belgian Institute for Space Aeronomy, Brussels, Belgium
[3]University of Chinese Academy of Sciences, Beijing, China

Correspondence: Minqiang Zhou (minqiang.zhou@aeronomie.be), Pucai Wang (pcwang@mail.iap.ac.cn)

Abstract. The column-averaged dry-air mole fractions of CO$_2$ (XCO$_2$), CH$_4$ (XCH$_4$) and CO (XCO) have been measured with a Bruker IFS 125HR Fourier transform infrared spectrometer (FTIR) at Xianghe (39.75 °N, 116.96 °E, North China) since June 2018. The site and the FTIR system are described in this study. The instrumental setup follows the guidelines of the Total Carbon Column Observing Network (TCCON), and the near-infrared spectra are recorded by an InGaAs detector together

5 with a CaF$_2$ beam splitter. The HCl cell measurements that are recorded regularly to derive the instrument line shape (ILS) show that the instrument is correctly aligned. The Xianghe site lies in a polluted area in North China where there are currently no TCCON sites. It can fill the TCCON gap in this region and expand the global coverage of the TCCON measurements. The TCCON standard retrieval code (GGG2014) is applied to retrieve XCO$_2$, XCH$_4$ and XCO. The time series, seasonal cycles and day-to-day variations of XCO$_2$, XCH$_4$ and XCO measurements at Xianghe between June 2018 and July 2019 are shown

10 and discussed. In addition, the FTIR measurements have been used to validate Orbiting Carbon Observatory-2 (OCO-2) and Tropospheric Monitoring Instrument (TROPOMI) satellite observations, as also shown in this paper. The Xianghe FTIR CO$_2$, CH$_4$ and CO data can be accessed at https://doi.org/10.18758/71021049 (Yang et al., 2019).

1 Introduction

The rapid economic growth of China has contributed to 30% of the global total carbon dioxide (CO$_2$) emissions from fossil

15 fuel consumption and cement production (Jackson et al., 2017). China dominates global CO$_2$ fossil emissions with an average increase of $3.8\%yr^{-1}$ between 2008 and 2017 (Le Quéré et al., 2018). In addition, 14% to 22% of the global anthropogenic methane (CH$_4$) emissions in the 2000s were attributed to China (Kirschke et al., 2013). It is clear that China should play an important role in the reduction of global carbon emission and climate change mitigation. A decreasing linear trend of -0.41 $\pm$ 0.09$\%yr^{-1}$ in carbon monoxide (CO) concentrations from 2005 to 2016 has been observed over East Asia and 76% of

20 this decrease is due to the CO emission control in China (Zheng et al., 2018). However, the estimation of Chinese carbon emissions still have large uncertainties, ranging from $\pm$ 5% to $\pm$ 10% (Gregg et al., 2008; Le Quéré et al., 2018; Andres et al.,

2012). A good understanding of carbon emissions requires accurate monitoring of CO_2, CH_4, CO and other direct and indirect greenhouse gases.

CO_2 is the most important anthropogenic greenhouse gas with a radiative forcing of 1.82 ± 0.19 W/m^2 in 2013 (IPCC, 2013). The globally averaged surface dry-air mole fraction of CO_2 increases steadily in the atmosphere since pre-industrial

5 times and has reached up to 405.5 ± 0.1 ppm in 2017 (WMO, 2018). The enhancement of CO_2 is primarily caused by human activities, such as the fossil burning and the land-use change (Peters et al., 2012). Atmospheric CH_4 is the second important anthropogenic greenhouse gas, and its globally averaged surface dry-air mole fraction increased up to 1859 ± 2 ppb in 2017 (WMO, 2018). Although the CH_4 abundance is much lower than that of CO_2, the comparative impact of CH_4 is about 28 times greater than CO_2 over a 100-year period (IPCC, 2013). It is reported that the radiative forcing of CH_4 has increased to $0.48 \pm$

10 0.05 W/m^2 in 2013 (IPCC, 2013). 50-65% of CH_4 is released from human activities such as energy production/consumption, industry, agriculture, biomass burning, and waste management activities and another 40% from natural emissions (IPCC, 2013). Atmospheric CO is an indirect greenhouse gas and is mainly emitted from fossil fuel combustion and biomass burning (Yin et al., 2015). There are mainly two methods to measure these three gases, in situ and remote sensing measurements including ground-based Fourier Transform Infrared (FTIR) measurements and satellite measurements that are discussed hereafter.

15 The Total Carbon Column Observing Network (TCCON) uses ground-based FTIR spectrometers to measure the direct solar radiation in the near infrared spectral region, from which the total column-averaged dry-air mole fractions of CO_2, CH_4, N_2O, CO, HF, H_2O and HDO are retrieved (Wunch et al., 2011b). Because of their relatively high precision and accuracy, TCCON data are widely used in satellite validations and model comparisons (Zhou et al., 2016; Ostler et al., 2016; Crisp et al., 2017; Borsdorff et al., 2018; Velazco et al., 2019). Today, there are 25 active TCCON sites (https://tccon-wiki.caltech.edu/)

20 covering the latitude band from 80 °N to 45 °S. Most TCCON sites are in North American, Europe, East Asia (South Korea and Japan) and Oceania. The Hefei station, located in Eastern China, is the first Chinese site that will potentially join the TCCON network. In 2016, a FTIR Bruker IFS 125HR instrument was installed at Xianghe (39.75 °N, 116.96 °E, 30m a.s.l.) and started observations following the TCCON settings in June 2018. As there are no TCCON sites in North China, the FTIR at Xianghe aims to fill the gap in the network in this region.

25 The Orbiting Carbon Observatory-2 (OCO-2) was launched on 2 July 2014 by NASA and is devoted to enhancing our understanding of regional scale CO_2 exchanges between the surface and the atmosphere (Crisp et al., 2004; Eldering et al., 2017; Crisp et al., 2017). The Tropospheric Monitoring Instrument (TROPOMI) was launched by ESA on 13 October 2017 as the single payload of the Sentinel-5 Precursor (S5P) satellite. It aims at providing accurate and timely observations of abundances of atmospheric species, such as CH_4 and CO, for air quality and climate change research and services (Borsdorff

30 et al., 2018). However, previous validation work (Wunch et al., 2017; Lambert et al., 2019) based on FTIR measurements has no study in North China due to the absence of TCCON sites in this area, so that it is important to add Xianghe site for evaluation of satellite products in this area.

In this paper, we describe the ground-based FTIR system at Xianghe, with a focus on the measurements of atmospheric CO_2, CH_4 and CO (Yang et al., 2019). The column-averaged dry-air mole fractions of these gases are retrieved by the GGG2014

35 (Wunch et al., 2015) code in the period between 14 June 2018 and 19 July 2019. The paper is structured as follows. Section 2

introduces the Xianghe site and the FTIR system. In Section 3, the retrieval and filtering methods are described. To increase the precision of the retrievals, the spectra are cloud filtered based on the separate direct solar irradiation measurements. The time series of XCO_2, XCH_4 and XCO are shown and discussed. In the next Section, the OCO-2 (XCO_2) and TROPOMI (XCH_4 and XCO) satellite observations are validated with the FTIR measurements at Xianghe. Finally, conclusions are drawn in Section
5   5.

2   FTIR measurements

2.1   Location and experimental set-up

Xianghe site has been operated by the Institute of Atmospheric Physics, Chinese Academy of Sciences since 1974. The site is about 50km to the east-southeast of Beijing and 70 km to the north-northwest of Tianjin (see Figure 1, right panel). The
10   Xianghe county acts as an integrated transportation and transfer center in Beijing-Tianjin-Hebei region, which is one of the most populous and economically dynamic areas in China (Ran et al., 2016). Xianghe has a middle latitude monsoon climate, with a prevailing south-east wind in summer and a north-west wind in winter (Song et al., 2011). The maximum temperature at Xianghe site is around 38 °C in summer, and the minimum temperature is around -10 °C in winter. The raining days occur mainly in summer including some days with extreme precipitations larger than 100 mm/day.

15   The Bruker IFS 125HR instrument was installed in the upper level of a four-story building in June 2016. About 2 years later, in June 2018, a solar tracker was installed on the roof (50 m a.s.l.), to guide the direct solar radiation into the FTIR instrument. The distance between the solar tracker and the entrance window of the FTIR instrument is about 3 meters. The solar tracker uses a camera inside the IFS 125HR spectrometer to ensure that the center of the solar disk always focuses on the entrance aperture of the spectrometer, with an active feedback loop. This system is set up following the developments from
20   Neefs et al. (2007) and Gisi et al. (2011). The FTIR operates only under clear-sky daytime conditions. A rain sensor and a solar irradiation (both total and direct) sensor, are installed next to the solar tracker, to monitor the weather conditions and to control the opening and closing of the solar tracker hatch. To protect the mirrors (Aluminum, coating with MgF_2) of the solar tracker, the hatch of the tracker automatically closes under rainy conditions and during nighttime. A heating system is operated in the tracker system to keep the temperature of the rotary stages and the mirrors close to 15°C in winter. Inside the lab, the
25   air-conditioning keeps the room temperature stabilized around 25 °C.

The near infrared (NIR) spectra are recorded by a indium gallium arsenide (InGaAs) detector and the middle infrared (MIR) spectra are recorded by a liquid nitrogen cooled indium antimonide (InSb) detector. The entrance window and the beamsplitter are made of CaF_2. The spectral ranges of the NIR and MIR spectra are 3800-11000 cm^{-1} and 2000-5000 cm^{-1}, respectively. The InSb detector at Xianghe records spectra in the AC mode. The InGaAs detector at Xianghe was operated in the AC
30   mode before 31 May 2019, but since then in the AC + DC mode to be compliant with TCCON standards. The spectrometer settings automatically alternate between NIR and MIR measurements during each clear-sky day. The entrance aperture of the spectrometer in the NIR spectrum is set to 0.5 mm and changed to 0.8 mm after 19 June 2019. There are approximately 70 NIR InGaAs for each clear day. The InGaAs spectra are recorded with a maximum optical path difference (MOPD) of 45cm,

corresponding to a spectral resolution of 0.02 cm^{-1}. Each measurement contains 2 scans (one forward and one backward), taking about 145 s.

About 50m south-west of the laboratory building, a weather station is operated on a 110m-height tower, at 62 meters above the ground, measuring pressure, temperature, humidity, wind direction and wind speed. The pressure sensor is located inside the LI-7550 Analyzer, which has an accuracy of 1 hPa. On 30 May 2019, a new weather station was installed at the same height as the solar tracker. The distance between the weather station and the solar tracker is about 2 meters. The pressure sensor is PTB210A Digital Barometer, with an accuracy of 0.07 hPa.

2.2 Instrument line shape

The instrument line shape (ILS) reflects the performance and alignment of the instrument (Schneider et al., 2008), which might be distorted by the shear or angular misalignment of the instrument or the field of view (FOV) (Hase et al., 1999; Wunch et al., 2015). A perfectly-aligned interferometer will perfectly center the Haidinger fringes on the field stop at all optical path differences (OPD). The offset between the moving cube-corner retro-reflector (CCRR) and the fixed CCRR will cause the Haidinger fringes moving away from the center when the mirror moves away from ZOPD and this is called shear misalignment. The angular misalignment is caused when the IR beam is not parallel to the rails. At Xianghe 2 HCl cell spectra are recorded every day after sunset. The modulation efficiency amplitude (ME) and phase error (PE) along the OPD are retrieved using the LINEFIT14.5 code (Hase et al., 1999). The ME is derived from the ratio of the misaligned fringe amplitude to the theoretical fringe amplitude. LINEFIT14.5 normalizes ME to be 1.0 at zero optical path difference (ZOPD). According to the TCCON requirement the ME changes must be within 5% and the PE must be less than 0.02 rad at MOPD (Wunch et al., 2011b). Figure 2 shows the time series of the ME and the PE at the MOPD (45 cm) at Xianghe. The last date ends on 31 March 2019 when the Tungsten lamp used to measure the HCl cell spectra broke down. The mean of the ME is 0.978 ± 0.004, and the mean of the PE is -0.008 ± 0.002 rad. Figure 2 shows that the alignment of the instrument slightly declines over time, but the ME and PE remain compliant with the TCCON requirements during the whole time period. A sensitivity study performed by Hase et al. (2013) showed that the uncertainty in XCO$_2$ is about 0.035% (0.14 ppm) for a ME change of 4%, which is within the 0.8 ppm (SZA less than 80 °) retrieval accuracy of TCCON XCO$_2$. Since the ME of the FTIR instrument at Xianghe is about 2-3%, the uncertainty from the ILS on the greenhouse gas retrievals can be ignored.

2.3 Signal-to-noise ratio

The time series of the signal-to-noise ratio (SNR) of the InGaAs spectra at Xianghe is shown in Figure 3. There are no measurements between 7 July and 22 August 2018 due to a power cut. The SNR decreases quickly with time because Xianghe is located in a polluted area (Robert and Richard, 2015; Li et al., 2007) causing rapid degradation of the mirrors of the solar tracker (Feist et al., 2016). In order to obtain a high SNR, the mirror of the solar tracker was cleaned on 14 November 2018 (first yellow line in Figure 3), with the SNR increased from 300 to 500. However, the SNR decreased back to the level of 300 about 3 weeks later, probably because of the increased level of air pollution and relatively lower solar irradiation in winter. The polluted mirror of the solar tracker was replaced with a new one on February 1, 2019 (second yellow line in Figure 3),

enhancing the SNR from about 300 to 450. With the DC signal recording (first red line in Figure 3), between May 31 2019 and June 19 2019 the SNR dropped quickly below 200. Therefore, the aperture size was increased from 0.5 to 0.8 mm on 19 June 2019 (second red line in Figure 3) and the mirror cleaned again on 25 June 2019 (third yellow line in Figure 3), making the SNR rise again above the level of 300.

3 FTIR retrievals

3.1 Retrieval Methodology

The non-linear least-squares fitting code GGG2014 (Wunch et al., 2015) is used to retrieve XCO_2, XCH_4, XCO and some other gases from the NIR solar absorption spectra at Xianghe.

$$TC_r = TC_a + \boldsymbol{A}(\boldsymbol{x_t} - \boldsymbol{x_a}) + \varepsilon, \tag{1}$$

where TC_a and TC_r are the a priori and retrieved total columns, $\boldsymbol{A}$ is the column averaging kernel, $\boldsymbol{x_t}$ and $\boldsymbol{x_a}$ are true and a priori partial column profiles, ε is the uncertainty. In the forward model, there are 70 equidistant 1km thick layers from the mean sea level up to 70km altitude. The a priori profiles of gases are generated by an empirical model based on surface in situ, ACE-FTS and MkIV measurements. The inter-annual trends and seasonal variations of the species are taken into account, and the a priori profiles are adjusted based on the local tropopause pressure at local noon (Toon and Wunch, 2015). The temperature, pressure and water vapour profiles are taken from the National Centres for Environmental Prediction (NCEP) reanalysis data (Kalnay et al., 1996). The surface pressure, temperature and water vapour are from the local weather station.

The column averaging kernel represents the vertical sensitivity of the retrieved total column to the true partial column profile. The typical averaging kernels of XCO_2, XCH_4 and XCO are shown in Figure 4 of Wunch et al. (2011a). In general, the retrieved CO_2 and CH_4 total columns have good sensitivity in the troposphere and the stratosphere. The retrieved CO column underestimates a deviation from the a priori partial column but overestimates a deviation from the a priori partial column in the stratosphere.

The retrieval windows of CO_2, CH_4, CO and O_2 are listed in Table 1 in Wunch et al. (2010). As an example, Figure 4 shows the residuals of the spectral fitting for CO_2 and O_2 for one NIR spectrum at a SZA of 22.9 °at Xianghe. The root mean square of the residuals for CO_2 in the spectral window 6180-6260cm^{-1}, CO_2 in the window 6297-6382 cm^{-1} and O_2 in the window 7765-8005 cm^{-1} are 0.24%, 0.25% and 0.37%, respectively, which compare well to the results in Toon et al. (2009).

The spectroscopy is the ATM line list (Toon, 2017). The total column-averaged dry-air mole fraction of gas (X_{gas}) is then derived from the ratio between the retrieved total column of the target species and the retrieved total column of O_2 and from the dry-air mole fraction of O_2 (0.2095)

$$X_{gas} = 0.2095 \times column_{gas}/column_{O_2}. \tag{2}$$

Using the ratio between the target species and O_2 reduces the uncertainties common to both gases, e.g., the surface pressure, water vapour, solar tracker pointing and zero level offsets. In addition, a post-processing of the results is done: (1) the airmass

dependence of the retrieval results which is known to be an artifact caused by spectroscopic uncertainties, is reduced by applying an empirical airmass-dependent correction, and (2) a constant scaling factor for each gas is applied to calibrate the TCCON measurements to the WMO scale (Wunch et al., 2015, 2010).

3.2 Data quality control

5   As the recording time for one InGaAs spectrum takes about 145 s, the stability of the incoming solar intensity during this period is important for the quality of the spectrum (Beer, 1992). If there are clouds or heavy aerosols in the light path between the FTS and the sun during the spectrum recording, the fractional line depth in FTIR spectra will be distorted (Ridder et al., 2011; Keppel-Aleks et al., 2011). To select the good quality spectra, we have discarded all the spectra with SNR less than 200.

The DC correction can be used to remove the solar irradiation variation in each spectrum (Keppel-Aleks et al., 2007). To filter

10   out spectra infected by the occurrence of clouds or high aerosol load before May 31, 2019 (in AC recording mode), we use the variations of the direct solar irradiation observed from the solar irradiation detector installed close to the solar tracker system (see Section 2.1). The solar direct irradiation is recorded every 3 seconds providing us with about 25 measurement points per forward or backward scan. If there are no clouds or strong loads of aerosol during the scan, the direct solar irradiation should remain relatively stable. We have classified measurement points during the scan as problematic if the solar intensity is

15   lower than a certain percentage threshold β of the maximum intensity. A spectrum is selected as a good one if the number of problematic measurement points is smaller than or equal a certain percentage threshold γ of the total number of measurement points during the measurement. We tested the filtering method with γ values of 0%, 5% and 10%, and β values of 85%, 90% and 95% on all InGaAs spectra (about 12000) from 14 June 2018 to 31 December 2018. The daily standard deviations (STD) of XCO_2, XCH_4 and XCO are calculated to compare with the expected random retrieval uncertainties. Note that only days

20   with more than 20 measurements per day are used to calculate the daily STD. The results are shown in Table 1. The STDs of XCO_2, XCH_4 and XCO decrease with increased β or decreased γ thresholds. The β and γ values are selected mainly based on the XCO_2 data. According to Wunch et al. (2015), the retrieved XCO_2 random uncertainty of TCCON data is about 0.2 % (0.8 ppm) with SZA less than 80 degrees. To reach this precision, the STD of our XCO_2 measurements should be less than 0.8 ppm, but at the same time, we try to keep the number of the measurements as large as possible. Therefore, we have chosen to

25   set $\beta = 90\%$ and $\gamma = 0\%$. This filtering, together with the SNR filter, makes us reach the required precision for TCCON XCO_2 also in the period before 31 May 2019.

The 110m-height meteorology tower is collinear with the solar irradiation sensor and the sun tracker. It generates a shadow on the mirror of the tracker system, affecting the spectra in the afternoon. The duration of the shadow is about 8-15 minutes, corresponding to about 2-3 InGaAs measurements. The shadow occurs at around 6:30 UTC (14:30 LTC) in summer and around

30   9:30 UTC (16:30 LTC) in winter. The upper panel in Figure 5 shows the solar direct intensity from 1 October 2018 to 3 October 2018, with a zoom in over the time period between 6:36 and 7:02 (UTC) on 2 October 2018 when the tower shadow is observed by the FTIR (see the inside camera image in the middle panel). The affected XCO_2 retrieval during the shadow appearing time are displayed in the bottom panel. The spectra sampling time is recorded at time of ZOPD. The blue dots in the upper panel denote the SNR of spectra filtered out with solar intensity (SI), the cyan dots denote the SNR of spectra filtered out with SNR,

and the red dots denote the SNR of spectra after both filtering. All of these SNR values are also zoomed in the middle panel of Figure 5. It is clear that the spectra polluted by the tower shadow can be filtered out by the combination of SNR filtering and SI filtering with $\beta = 90$ % and $\gamma = 0$ % (see cyan and blue dots in middle panel, appearing in the same period with the shadow). The other blue dots in the upper panel appearing outside the shadow shows that SI filtering can also filter out spectra which are

5   polluted by clouds.

Figure 6 shows the time series of XCO_2 with and without filtering between 14 June 2018 and 19 July 2019. In the bottom panel, the cyan dots denote all the XCO_2 values before any filtering, the blue dots denote the XCO_2 values after SNR filtering applied and the red dots denote the XCO_2 values after both SNR and SI filtering have been applied. In the upper panel, the blue dots denote the daily STDs of XCO_2 when only the SNR filtering is applied, while the red ones denote the daily STDs

10   of XCO_2 when both the SNR and the SI filtering are applied. Table 2 shows that SNR filtering apparently reduces the average daily STDs both before (from 1.39 ppm to 1.14 ppm) and after (from 1.34 ppm to 0.76 ppm) DC signal recording. It is clear that before 31 May 2019, more XCO_2 outliers are removed by the SI filtering, with the average daily STD of XCO_2 decreasing from 1.14 ppm to 0.71 ppm. After 31 May 2019, the SNR filtering already discards most of the bad spectra, and the average XCO_2 daily STDs with SNR filtering and SNR + SI filtering are 0.76 ppm and 0.83 ppm, respectively in this period. The DC

15   signal can help to reduce the influence from clouds and the tower, thus the SI filtering has little influence to these data. In following analysis, we only use the data after both SNR and SI filtering for the whole period.

Poor instrument alignment, spectral ghost, error in the time assigned to the spectrum or faulty pressure sensor may cause a dramatic jump in X_{air} (Washenfelder et al., 2006; Wunch et al., 2011a). The retrieved X_{air} (after both SNR and SI filtering) are shown in Figure 7 to confirm the good quality of the retrievals. X_{air} is defined as

20   $$X_{air} = \frac{TC_{dry,air}}{TC_{O_2}/0.2095} = \frac{0.2095}{TC_{O_2}} \left[\frac{P_s}{gm_{dry,air}} - TC_{H_2O} \frac{m_{H_2O}}{m_{dry,air}} \right], \tag{3}$$

where $m_{dry,air}$ and m_{H_2O} are the molecular mass of dry air and water vapour and g is the column-averaged gravitational acceleration, P_s is the surface pressure and $TC_{dry,air}$, TC_{O_2} and TC_{H_2O} are total columns of dry air, O_2 and H_2O, respectively. The X_{air} is around 0.98 due to a 2.0% bias in the O_2 spectroscopy (Kivi and Heikkinen, 2016). Figure 7 shows that the X_{air} at Xianghe all pass TCCON standard quality check (between 0.96 and 1.04) and is stable over time with a mean value of 0.982

25   and a STD of 0.003.

3.3   Retrieval results and discussions

The time series of XCO_2, XCH_4 and XCO after both SNR and SI filtering from June 2018 to July 2019 are shown in Figure 8. The monthly mean of XCO_2, XCH_4 and XCO at Xianghe, Pasadena (34.1°N) (Wennberg et al., 2014), Lamont (36.6°N) (Wennberg et al., 2016) and Karlsruhe (49.1°N) (Hase et al., 2014) from June 2018 are also displayed in Figure 9. Based on

30   these measurements, the seasonal variations and day-to-day variations of XCO_2, XCH_4 and XCO are assessed.

XCO_2 is low in summer and high in winter and spring at Xianghe, with maximum monthly mean 414.27 ± 0.94 ppm in April and minimum monthly mean 401.58 ± 1.32 ppm in August. This seasonal behaviour is similar to those at Pasadena, Lamont and Karlsruhe, which are located in the northern mid-latitude zone. The peak-to-peak amplitude of the seasonal variation of

XCO_2 (computed as the difference between the maximum monthly mean and minimum monthly mean) is 12.41 ppm, which is larger than 7.45 ppm at Pasadena, 7.78 ppm at Lamont and 7.98 ppm at Karlsruhe. XCH_4 is low in spring and high in autumn and summer, with a maximum monthly mean 1.893 ± 0.017 ppm in August and a minimum monthly mean 1.857 ± 0.014 ppm in March. It is found that the seasonal cycle of the XCH_4 at Xianghe is very different with other sites at a similar latitude, as the observations at the other 3 stations show low values in summer and high values in autumn and winter (Figure 9, middle panel). The peak-to-peak amplitude of the seasonal variation is about 0.039 ppm, which is also larger than 0.029 ppm at Pasadena, 0.028 ppm at Lamont and 0.024 ppm at Karlsruhe. XCO at Xianghe is relatively high during the whole year. The background value of XCO is about 90 ppb, and the high XCO measurements can reach up to 200 ppb. The monthly mean XCO values at Xianghe are always higher than those at the other 3 stations (Figure 9, lower panel), indicating that regional pollution sources are frequently observed at Xianghe.

Similar day-to-day variations are observed among XCO_2, XCH_4 and XCO. For example, the mole fractions of these three species increase together from 8 to 12 January 2019 and drop down on 13 January 2019 (see Figure 10). The high values are related to the local emissions while the low values are influenced by the air transported from remote places. Back trajectories of 72 hours at Xianghe are shown in Figure 11 using the Hybrid Single-Particle Lagrangian Integrated Trajectory (HYSPLIT) model. The air is released at altitudes of 500, 2000 and 5000 m a.g.l. at local noon on 8, 12 and 13 January 2019. The Meteorological data are from NCEP Global Forecast System, with a horizontal resolution of 0.5°×0.5°and 55 hybrid sigma-pressure levels. Figure 11 shows that the air arriving at Xianghe are mainly coming from the west and north during this period. The emission sources are mainly influencing the air arriving at 500 m altitude above Xianghe: on 8 and 13 January 2019 these are mainly coming from the north-west of Xianghe with a relative fast wind speed, while on 12 January 2019 they are mainly coming from the west of Xianghe with a much slower wind speed. As shown in Figure 1, Beijing is situated west of Xianghe, and the mountains are located at the west and north of Beijing. The air in the lower troposphere on 12 January 2019 is strongly affected by the strong local pollution, while the air arriving on 8 and 13 January 2019 are originating in relatively clean places (Inner Mongolia and Mongolia).

4 Satellite validation

4.1 Methodology

In this section, the FTIR XCO_2, XCH_4 and XCO measurements at Xianghe are used to validate the OCO-2 XCO_2 and TROPOMI XCH_4 and XCO satellite observations. The co-located FTIR-satellite data pairs are selected based on spatial-temporal collocation criteria. The detailed selection criteria for each target (OCO-2 XCO_2, TROPOMI XCH_4 and TROPOMI XCO) are described in the subsections 4.2 and 4.3: they account for the scan width of the satellite instrument and the characteristics of the target species.

According to Rodgers and Connor (2003), the differences in a priori profiles should be taken into account when comparing ground-based FTIR and satellite observations. TCCON CO_2, CH_4 and CO a priori profiles (70 layers) have been discussed in Section 3.1. OCO-2 CO_2 a priori profiles (19 layers) are created based on the GLOBALVIEW dataset and change with

time and location (O'Dell et al., 2012). TROPOMI uses the global chemical transport model TM5 to get CH_4 and CO a priori profiles (12 layers) (Borsdorff et al., 2018; Hasekamp et al., 2019). The TM5 model data are monthly means with a horizontal resolution of 3°latitude ×2°longitude and 60 vertical levels (Krol et al., 2005). In this study, the satellite a priori profile (OCO-2 or TROPOMI) is taken to be the common a priori profile in the comparison. To substitute the satellite a priori profile in the

5 FTIR retrieval we follow Rodgers and Connor (2003):

$$X'_{FTIR} = X_{FTIR} + (\boldsymbol{A} - \boldsymbol{I})(\boldsymbol{x}_{a,FTIR} - \boldsymbol{x}_{a,SAT}), \tag{4}$$

where X'_{FTIR} is the FTIR retrieved total column using the satellite a priori profile, X_{FTIR} is the original FTIR retrieval, $\boldsymbol{A}$ is the FTIR TCCON column averaging kernel, $\boldsymbol{x}_{a,FTIR}$ and $\boldsymbol{x}_{a,SAT}$ are the a priori partial column profiles of FTIR and satellite retrievals, respectively. As the vertical layering of the FTIR retrieval is different from that of the satellite retrieval (OCO-2 or

10 TROPOMI), the satellite a priori profile is re-gridded to the FTIR layer. After re-gridding, the total a priori column remains unchanged (Langerock et al., 2015).

To compare the FTIR and satellite column measurements, the satellite measurements are corrected for a possible difference between the altitudes of its ground pixel and that of the FTIR site at Xianghe. If the surface altitude of the satellite footprint is higher than the altitude of the FTIR instrument, the FTIR a priori profile ($\boldsymbol{x}_{a,FTIR}$) is used to fill the gap between the

15 satellite lowest level ($P_{s,SAT}$) and the FTIR height ($P_{s,FTIR}$), otherwise the satellite a priori profile is considered to be the profile between the satellite lowest level and the FTIR height. Then the partial column of dry air ($PC_{dry,air}$) or target species (PC_{gas}) between the satellite footprint surface altitude and the FTIR surface altitude is calculated as

$$PC_{dry,air} = \int_{P_{s,SAT}}^{P_{s,FTIR}} \frac{dP}{g_{(P)}(m_{dry,air} + m_{h2o}\overline{\nu}_{h2o})}, \tag{5}$$

20 $$PC_{gas} = \int_{P_{s,SAT}}^{P_{s,FTIR}} \frac{dP}{g_{(P)}(m_{dry,air} + m_{h2o}\overline{\nu}_{h2o})} x_{(P)}, \tag{6}$$

where $g_{(P)}$ is gravitational acceleration at height P, $x_{(P)}$ is the a priori VMR profile of each target gas, $\overline{\nu}_{h2o}$ is the VMR of water vapor in the dry air, calculated as

$$\overline{\nu}_{h2o} = \frac{\nu_{h2o}}{1 - \nu_{h2o}}, \tag{7}$$

where ν_{h2o} is the VMR of water vapor in the wet air. Then each satellite pixel measurement is scaled with one scaling factor

25 (α) related to satellite pixel level, which is computed as

$$\alpha = \frac{(TC_{gas}^{SAT} + PC_{gas})}{TC_{gas}^{SAT}} \bigg/ \frac{(TC_{dry,air}^{SAT} + PC_{dry,air})}{TC_{dry,air}^{SAT}}, \tag{8}$$

where $TC_{dry,air}^{SAT}$ and TC_{gas}^{SAT} are the total column of dry air and target species in the satellite measurement column. The random error of FTIR measurements together with the systematic and random errors of satellite measurements are considered here for the comparison.

4.2 OCO-2

OCO-2 incorporates three imaging grating spectrometers to measure near-infrared spectra. The spectral resolution of OCO-2 is approximately 20 times lower than that of the TCCON FTIR (0.02 cm^{-1}) instruments (Frankenberg et al., 2015). OCO-2 collects 8 soundings over its 0.8°swath width every 0.333s with a 16-day repeat cycle (https://ocov2.jpl.nasa.gov/observatory/instrument/). The OCO-2 XCO_2 measurements are retrieved by the ACOS retrieval algorithm (O'Dell et al., 2012), based on the optimal estimation method. Three bands (0.756 μm, 1.61μm and 2.06 μm) are used in the XCO_2 retrieval. The a priori surface pressure, profiles of temperature and water vapor are from 3-hourly ECMWF model forecast fields and linearly interpolated in space and time to the satellite footprint. Note that there are three versions (v7, v8 and v9) available on the NASA website for the OCO-2 data. Each version comes in two variants: full and lite. The full variant contains all the retrieved parameters, but without any post-correction applied to the data. The lite variant only includes some important parameters, but the data are corrected in terms of a footprint-dependent bias, a parameter-dependent bias and a scaling bias according to the WMO trace-gas standard scale. Compared to v7, many parameters have been improved in v8, such as latitude-dependent problems, surface model, spectroscopy, potential instrumental problems, atmospheric scattering by clouds and aerosols, a spatial-temporal sampling error of a priori surface pressure and the systematic pointing offsets (O'Dell et al., 2012). Based on v8, v9 has a better estimation of the surface pressure, and it shows a better performance in regions with rough topography such as over Lauder (New Zealand) (Kiel et al., 2019). In this study, the latest v9 lite data are selected (https://ocov2.jpl.nasa.gov).

The satellite measurements are selected within 5° latitude × 10° longtitude around Xianghe, these are the same criteria as adopted by Wunch et al. (2017). For each FTIR measurement, the nearby satellite measurement in the spatial collocation box, with less than 2-hours' measurement time difference, is chosen to form one FTIR-satellite data pair. Note that there are nadir and glint observational modes of OCO-2 measurements over Xianghe, and these two types of measurements are combined together to get a statistically robust result because of the limited number (28 days) of data pairs.

The time series of the collocated OCO-2 and ground-based FTIR data from 27 June 2018 to 31 May 2019 (last date of satellite data availability) is shown in Figure 12. To avoid the influence from the cloud, we select the co-located data pair, which has at least 20 OCO-2 measurements within the box. The upper panel in Figure 12 (left) shows the daily mean bias of measured XCO_2 from OCO-2 and FTIR. The mean of OCO-2 measurements is 0.62 ppm lower than that of the FTIR measurements, with a STD of 1.20 ppm. The absolute differences between OCO-2 v9 lite data and Xianghe FTIR data are comparable with the results found for the v7 lite products in Wunch et al. (2017) for other TCCON stations with biases ranging from -0.7 ± 1.32 ppm (Wollongong) to 0.9 ± 1.49 ppm (Karlsruhe) in land glint mode and ranging from -0.1 ± 1.04 ppm (Wollongong) to 1.6 ± 2.05 ppm (Garmisch) in nadir mode. The scatter plot of OCO-2 and FTIR at Xianghe is shown in the right panel in Figure 12: the derived correlation coefficient (R) is 0.959. We can conclude that OCO-2 data are in good agreement with the Xianghe FTIR data, and in particular, that OCO-2 captures the seasonal cycle of XCO_2 at Xianghe, with a maximum in winter-spring and a minimum in late summer.

4.3 TROPOMI

In this section, the TROPOMI XCH$_4$ and XCO are compared with the FTIR measurements at Xianghe. TROPOMI is a grating spectrometer measuring solar radiation reflected by the Earth and observes in the ultraviolet and visible, near-infrared and shortwave infrared spectral regions. It has a wide swath of around 2600 km across the track and a daily global coverage of the
5 Earth. The spatial resolution of TROPOMI is about 7km × 7km before 6 August 2019 and then it changes to 7.2km × 5.6km. The TROPOMI CO data are provided in three different data streams: the near-real-time (NRTI) stream, the Offline stream (OFFL) and the Reprocessing (RPRO) stream (Landgraf et al., a). CH$_4$ data are provided in bias-corrected and not-corrected versions (Landgraf et al., b). In our validation, we considered the off-line and reprocessed CO data, from processor versions 01.02 and higher. For CH$_4$, we also look at bias-corrected data with processor versions of 01.02 and higher.

10 TROPOMI uses the RemoTeC algorithm to retrieve CH$_4$ column using the 0.757-0.774 µm O$_2$ absorption band and 2.305-2.385 µm CH$_4$ absorption band (Hasekamp et al., 2019). The requirements for the accuracy and precision for TROPOMI XCH$_4$ are 1% and 1.5%, respectively (Hasekamp et al., 2019). We select TROPOMI XCH$_4$ measurements that occur within 1 hour of FTIR measurements and within a distance of 100 km from the Xianghe station based on the collocation criteria adopted at other TCCON sites (Lambert et al., 2019). In agreement with Landgraf et al. (b), the TROPOMI pixels are selected with
15 a quality assurance value above 0.5, which removes pixels with processing errors, anomalously high signals and increasing specular reflection of sunlight by the sea surface (Hasekamp et al., 2019). Similar to OCO-2, to reduce the influence from the clouds, we only select the days when there are at least 5 co-located TROPOMI CH$_4$ pixels.

The left panel in Figure 13 shows the time series of co-located TROPOMI and FTIR XCH$_4$ daily means and their relative biases (%,(satellite-FTIR)/FTIR) from 27 June 2018 to 19 July 2019 (86 days). The mean bias is -0.60 %, which is within the
20 S5P validation requirement of a bias of 1%. In addition, the STD of the relative biases is 0.55 %, which also meets the S5P mission requirement of 1.5% (Lambert et al., 2019). The R between TROPOMI and FTIR XCH$_4$ daily means is 0.834 (Figure 13, right panel). According to the TROPOMI validation report (Lambert et al., 2019), the bias at Xianghe is comparable to the ones at Tsukuba, Lamont and Rikubetsu (similar latitude band).

The TROPOMI XCO measurements are retrieved from the SICOR algorithm (Hasekamp et al., 2019) in the 2.3 µm spectral
25 range. The retrieved TROPOMI CO data is in the unit of total column density (molecules/cm^2), so we converted them to to XCO (ppb) values for comparison with FTIR XCO measurements. Because CO is relatively reactive compared to CH$_4$, we must reduce the measurement time and location differences in the colocation criteria. Therefore, the TROPOMI observations are selected within 30 minutes of each FTIR measurement and within a maximum distance of 50 km away from the FTIR site and along the light path of the ground-based FTIR measurements. Similar to CH$_4$, we only select the days when there
30 are at least 5 co-located TROPOMI CO pixels. In addition, to reduce the impact from long light paths through the atmosphere (Landgraf et al., a), the TROPOMI measurements with a SZA larger than 80°or a satellite zenith angle larger than 65°are filtered out. And we only select the TROPOMI CO products in clear sky cases with cloud height below 500 m and cloud optical depth < 0.5.

The left panel of Figure 14 shows the time series and relative biases of co-located TROPOMI and FTIR XCO daily means at Xianghe from 27 June 2018 to 31 May 2019 (70 days). The mean bias and STD between TROPOMI and FTIR are 2.05% and 7.82%, respectively, which are within the S5P mission requirement (bias < 15% and STD < 10%). Compared to other TCCON sites(Lambert et al., 2019), the mean relative bias is quite lower, which is because high pollution events are frequently observed at Xianghe while the satellite CO partial column a priori profile is under-estimated in the lower troposphere over Xianghe. The good agreement between TROPOMI and FTIR XCO with a R of 0.961 (Figure 14, right panel) highlights the good performance of TROPOMI over Xianghe.

5 Conclusions

A new atmospheric ground-based FTIR site equipped with a Bruker IFS 125HR has been in operation since 14 June 2018 at Xianghe in North China. The NIR spectra are recorded following the TCCON operation procedures. As it is a rather polluted location, it can provide useful information for the study of the carbon cycle in North China and the validation of related satellite observations. Regular HCl cell measurements show that the ME loss is within 2% and the PE remains within 0.02 rad, confirming the ILS of the FTIR is well aligned and meets the TCCON requirement.

XCO_2, XCH_4 and XCO have been retrieved using the TCCON standard algorithm GGG2014. The InGaAs spectra have been recorded in AC mode before 31 May 2019 and AC+DC mode since then: the SNR and SI filtering are applied for both periods, about 85% spectra are selected as the good spectra. The uncertainty of the retrieved XCO_2 at both time periods keep consistent (about 0.8 ppm; close to the TCCON uncertainty), reflecting that the SI filtering can overcome the absence of the DC signal in the first period.

A clear seasonal variation of XCO_2 has been observed during this 1-year period of measurements, with lowest values of 401.58 ± 1.32 ppm in summer and highest values of 414.27 ± 0.94 ppm in winter. Low XCH_4 concentrations are observed in spring (1.857 ± 0.014 ppm) and high values in autumn and summer (1.893 ± 0.017 ppm). For XCO there is no clear seasonal variation, but a large day-to-day variability. A case study based on the HYSPLIT back trajectories of 72 h at Xianghe from 8 January 2019 to 13 January 2019 shows that short-term increases of XCO_2, XCH_4 and XCO can be traced back to local emissions.

The XCO_2, XCH_4 and XCO FTIR measurements at Xianghe provide useful information for related satellite validation in North China. The mean bias between FTIR and OCO-2 XCO_2 measurements is -0.62 ppm with a STD of 1.20 ppm. The mean and STD of the relative differences between FTIR and TROPOMI XCH_4 measurements are -0.60% and 0.55%, respectively. The mean and STD of the relative differences between FTIR and TROPOMI XCO measurements are 2.05% and 7.82%, respectively. Our measurements show that these satellite observations have good performance in this region.

In summary, this study shows that the Xianghe data comply with the TCCON specifications and we aim to become a part of TCCON in future.

6 Data availability

The Xianghe FTIR CO_2, CH_4 and CO data can be accessed at https://doi.org/10.18758/71021049 (Yang et al., 2019). The OCO-2 data are publicly available (https://ocov2.jpl.nasa.gov). The TROPOMI data are publicly available (https://scihub.copernicus.eu/).

Author contributions. MZ, PW, GW and MDM desgined the experiment. YY, MZ, CH,TW, DJ, CV, NK operated and maintained the FTIR

5 instruments. YY, MZ, BL and MKS performed the satellite validation. YY and MZ worte the manuscript and all authors read and provided comments on the paper.

Competing interests. The authors declare that they have no conflict of interest.

Acknowledgements. The work is supported by National Key R & D Program of China (Nos. 2017YFB0504000 and 2017YFC1501701), the National Natural Science Foundation of China (No.41575034) and China Scholarship Council. We want to thank TCCON community for

10 sharing the retrieval code GGG2014. We also want to thank Weidong Nan, Qun Cheng and Qing Yao at Xianghe site, Rongshi Zou (IAP) and Francis Scolas for the FTIR maintenance.

References

Andres, R. J., Boden, T. A., Bréon, F.-M., Ciais, P., Davis, S., Erickson, D., Gregg, J. S., Jacobson, A., Marland, G., Miller, J., Oda, T., Olivier, J. G. J., Raupach, M. R., Rayner, P., and Treanton, K.: A synthesis of carbon dioxide emissions from fossil-fuel combustion, Biogeosciences, 9, 1845–1871, https://doi.org/10.5194/bg-9-1845-2012, 2012.

5 Beer, R.: Remote Sensing by Fourier Transform Spectrometry, Wiley-Interscience, New York, 120, 1992.

Borsdorff, T., Aan de Brugh, J., Hu, H., Aben, I., Hasekamp, O., and Landgraf, J.: Measuring Carbon Monoxide With TROPOMI: First Results and a Comparison With ECMWF-IFS Analysis Data, Geophys. Res. Lett., 45, 2826–2832, https://doi.org/10.1002/2018GL077045, 2018.

Crisp, D., Atlas, R., Breon, F.-M., Brown, L., Burrows, J., Ciais, P., Connor, B., Doney, S., Fung, I., Jacob, D., Miller, C., O'Brien, D.,
10 Pawson, S.and Randerson, J., Rayner, P., Salawitch, R., Sander, S., Sen, B., and et al.: The Orbiting Carbon Observatory (OCO) mission, Adv. Space. Res., 34, 700–709, https://doi.org/10.1016/j.asr.2003.08.062, 2004.

Crisp, D., Pollock, H. R., Rosenberg, R., Chapsky, L., Lee, R. A. M., Oyafuso, F. A., Frankenberg, C., O'Dell, C. W., Bruegge, C. J., Doran, G. B., Eldering, A., Fisher, B. M., Fu, D., Gunson, M. R., Mandrake, L., B., O. G., Schwandner, F. M., Sun, K., Taylor, T. E., Wennberg, P. O., and Wunch, D.: The on-orbit performance of the Orbiting Carbon Observatory-2 (OCO-2) instrument and its radiometrically
15 calibrated products, Atmos. Meas. Tech., 10, 59–81, https://doi.org/10.5194/amt-10-59-2017, 2017.

Eldering, A., O'Dell, C. W., Wennberg, P. O., Crisp, D., Gunson, M. R., Viatte, C., Avis, C., Braverman, A., Castano, R., Chang, A., Chapsky, L., Cheng, C., Connor, B., Dang, L., Doran, G., Fisher, B., Frankenberg, C., Fu, D., Granat, R., Hobbs, J., Lee, R. A. M., Mandrake, L., McDuffie, J., Miller, C. E., Myers, V., Natraj, V., O'Brien, D., Osterman, G. B., Oyafuso, F., Payne, V. H., Pollock, H. R., Polonsky, I., Roehl, C. M., Rosenberg, R., Schwandner, F., Smyth, M., Tang, V., Taylor, T. E., To, C., Wunch, D., and Yoshimizu, J.: The Orbiting
20 Carbon Observatory-2: first 18 months of science data products, Atmos. Meas. Tech., 10, 549–563, https://doi.org/10.5194/amt-10-549-2017, 2017.

Feist, D. G., Arnold, S. G., Hase, F., and Ponge, D.: Rugged optical mirrors for Fourier transform spectrometers operated in harsh environments, Atmos. Meas. Tech., 9, 2381–2391, https://doi.org/10.5194/amt-9-2381-2016, 2016.

Frankenberg, C., Pollock, R., Lee, R. A. M., Rosenberg, R., Blavier, J.-F., Crisp, D., O'Dell, C. W., Osterman, G. B., Roehl, C., Wennberg,
25 P. O., and Wunch, D.: The Orbiting Carbon Observatory (OCO-2): spectrometer performance evaluation using pre-launch direct sun measurements, Atmos. Meas. Tech., 8, 301–313, https://doi.org/10.5194/amt-8-301-2015, 2015.

Gisi, M., Hase, F., Dohe, S., and Blumenstock, T.: Camtracker: a new camera controlled high precision solar tracker system for FTIR-spectrometers, Atmos. Meas. Tech., 4, 47–54, https://doi.org/10.5194/amt-4-47-2011, 2011.

Gregg, J. S., Andres, R. J., and Marland, G.: China: Emissions pattern of the world leader in CO2 emissions from fossil fuel consumption
30 and cement production, Geophys. Res. Lett., 35, https://doi.org/10.1029/2007GL032887, 2008.

Hase, F., Blumenstock, T., and Paton-Walsh, C.: Analysis of the instrumental line shape of high-resolution Fourier transform IR spectrometers with gas cell measurements and new retrieval software, Appl. Opt., 38, 3417–3422, https://doi.org/10.1364/AO.38.003417, 1999.

Hase, F., Drouin, B. J., Roehl, C. M., Toon, G. C., Wennberg, P. O., Wunch, D., Blumenstock, T., Desmet, F., Feist, D. G., Heikkinen, P., De Mazière, M., Rettinger, M., Robinson, J., Schneider, M., Sherlock, V., Sussmann, R., Té, Y., Warneke, T., and Weinzierl, C.: Calibration
35 of sealed HCl cells used for TCCON instrumental line shape monitoring, Atmos. Meas. Tech., 6, 3527–3537, https://doi.org/10.5194/amt-6-3527-2013, 2013.

Hase, F., Blumenstock, T., Dohe, S., Gross, J., and Kiel, M.: TCCON data from Karlsruhe (DE), Release GGG2014R0, TCCON data archive, hosted by CaltechDATA, https://doi.org/10.14291/tccon.ggg2014.karlsruhe01.R0/1149270, https://tccondata.org, 2014.

Hasekamp, O., Lorente, A., Hu, H., Butz, A., de Brugh, J., and Landgraf, J.: Algorithm Theoretical Baseline Document for Sentinel-5 Precursor Methane Retrieval, Netherlands Institute for Space Research, p. 67, http://www.tropomi.eu/sites/default/files/files/publicSentinel-5P-TROPOMI-ATBD-Methane-retrieval.pdf, 2019.

IPCC: Climate change 2013: The physical science basis, Contribution of Working Group I to the Fifth Assessment Report of the Intergovernmental Panel on Climate Change, https://www.ipcc.ch/report/ar5/wg1/, 2013.

Jackson, R. B., Le Quéré, C., Andrew, R. M., Canadell, J. G., Peters, G. P., Roy, J., and Wu, L.: Warning signs for stabilizing global CO2 emissions, Environ. Res. Lett., 12, https://doi.org/10.1088/1748-9326/aa9662, 2017.

Kalnay, E., Kanamitsu, M., Kistler, R., Collins, W., Deaven, D., Gandin, L., Iredell, M., Saha, S., White, G., Woollen, J., Zhu, Y., Chelliah, M., Ebisuzaki, W., Higgins, W., Janowiak, J., Mo, K. C., Ropelewski, C., Wang, J., Leetmaa, A., Reynolds, R., Jenne, R., and Joseph, D.: The NCEP/NCAR 40-Year Reanalysis Project, B. Am. Meteorol. Soc., 77, 437–472, https://doi.org/10.1175/1520-0477(1996)077<0437:TNYRP>2.0.CO;2, 1996.

Keppel-Aleks, G., Toon, G. C., Wennberg, P. O., and Deutscher, N. M.: Reducing the impact of source brightness fluctuations on spectra obtained by Fourier-transform spectrometry, Appl. Opt., 46, 4774–4779, https://doi.org/10.1364/AO.46.004774, 2007.

Keppel-Aleks, G., Wennberg, P. O., and Schneider, T.: Sources of variations in total column carbon dioxide, Atmos. Chem. Phys., 11, 3581–3593, https://doi.org/10.5194/acp-11-3581-2011, 2011.

Kiel, M., O'Dell, C. W., Fisher, B., Eldering, A., Nassar, R., MacDonald, C. G., and Wennberg, P. O.: How bias correction goes wrong: measurement of X_{CO_2} affected by erroneous surface pressure estimates, Atmos. Meas. Tech., 12, 2241–2259, https://doi.org/10.5194/amt-12-2241-2019, 2019.

Kirschke, S., Bousquet, P., Ciais, P., Saunois, M., Canadell, J. G., Dlugokencky, E. J., Bergamaschi, P., Bergmann, D., D.R., B., Bruhwiler, L., Cameron-Smith, P., Castaldi, S., Chevallier, F., Feng, L., Fraser, A., M., H., Hodson, E. L., Houweling, S., Josse, B., Fraser, P. J., and et al.: Three decades of global methane sources and sinks, Nat. Geosci., pp. 813–823, https://doi.org/10.1038/ngeo1955, 2013.

Kivi, R. and Heikkinen, P.: Fourier transform spectrometer measurements of column CO_2 at Sodankylä, Finland, Geosci. Instrum. Method. Data Syst., 5, 271–279, https://doi.org/10.5194/gi-5-271-2016, 2016.

Krol, M., Houweling, S., Bregman, B., van den Broek, M., Segers, A., van Velthoven, P., Peters, W., Dentener, F., and Bergamaschi, P.: The two-way nested global chemistry-transport zoom model TM5: algorithm and applications, Atmos. Chem. Phys., 5, 417–432, https://doi.org/10.5194/acp-5-417-2005, 2005.

Lambert, J. C., Keppens, A., Hubert, D., Langerock, B., Eichmann, K., Kleipool, Q., Sneep, M., Verhoelst, T., Wagner, T., Weber, M., Ahn, C., Argyrouli, A., Balis, D., Chan, K., Compernolle, S., De Smedt, I., Eskes, H., Fjæraa, A., Garane, K., and et al.: Quarterly Validation Report of the CopernicusSentinel-5 PrecursorOperational Data Products–#03:July2018–May2019, S5P MPC Routine Operations Consolidated Validation Reportseries, 3, 1–125, http://www.tropomi.eu/sites/default/files/files/publicS5P-MPC-IASB-ROCVR-03.0.1-20190621_FINAL.pdf, 2019.

Landgraf, J., Borsdorff, T., Langerock, B., and Keppens, A.: S5P Mission Performance Centre Carbon Monoxide [L2__CO____] Readme, http://www.tropomi.eu/sites/default/files/files/publicS5P-MPC-SRON-PRF-CO_v01.03.02_1.2_20190703.pdf, accessed: 2019-07-03, a.

Landgraf, J., Lorente, A., Langerock, B., and Sha, M. K.: S5P Mission Performance Centre Methane [L2__CH4___] Readme, http://www.tropomi.eu/sites/default/files/files/publicSentinel-5P-Methane-Product-Readme-File.pdf, accessed: 2019-02-28, b.

Langerock, B., De Mazière, M., Hendrick, F., Vigouroux, C., Desmet, F., Dils, B., and Niemeijer, S.: Description of algorithms for co-locating and comparing gridded model data with remote-sensing observations, Geosci. Model Dev., 8, 911–921, https://doi.org/10.5194/gmd-8-911-2015, 2015.

Le Quéré, C., Andrew, R. M., Friedlingstein, P., Sitch, S., Hauck, J., Pongratz, J., Pickers, P. A., Korsbakken, J. I., Peters, G. P., Canadell, J. G., Arneth, A., Arora, V. K., Barbero, L., Bastos, A., Bopp, L., Chevallier, F., Chini, L. P., Ciais, P., Doney, S. C., Gkritzalis, T., Goll, D. S., Harris, I., and et al.: Global Carbon Budget 2018, Earth Syst. Sci. Data., 10, 2141–2194, https://doi.org/10.5194/essd-10-2141-2018, 2018.

Li, Z. Q., Xia, X. A., Cribb, M., Mi, W., Holben, B., Wang, P. C., Chen, H. B., Tsay, S., Eck, T. F., Zhao, F. S., Dutton, E. G., and Dickerson, R. E.: Aerosol optical properties and their radiative effects in northern China, J. Geophys. Res. Atmos., 112, https://doi.org/10.1029/2006JD007382, 2007.

Neefs, E., De Mazière, M., Scolas, F., Hermans, C., and Hawat, T.: BARCOS, an automation and remote control system for atmospheric observations with a Bruker interferometer, Rev. Sci. Instrum., 78, https://doi.org/10.1063/1.2437144, 2007.

O'Dell, C. W., Connor, B., Bösch, H., O'Brien, D., Frankenberg, C., Castano, R., Christi, M., Eldering, D., Fisher, B., Gunson, M., McDuffie, J., Miller, C. E., Natraj, V., Oyafuso, F., Polonsky, I., Smyth, M., Taylor, T., Toon, G. C., Wennberg, P. O., and Wunch, D.: The ACOS CO_2 retrieval algorithm – Part 1: Description and validation against synthetic observations, Atmos. Meas. Tech., 5, 99–121, https://doi.org/10.5194/amt-5-99-2012, 2012.

Ostler, A., Sussmann, R., Patra, P. K., Houweling, S., De Bruine, M., Stiller, G. P., Haenel, F. J., Plieninger, J., Bousquet, P., Yin, Y., Saunois, M., Walker, K. A., Deutscher, N. M., Griffith, D. W. T., Blumenstock, T., Hase, F., Warneke, T., Wang, Z., Kivi, R., and Robinson, J.: Evaluation of column-averaged methane in models and TCCON with a focus on the stratosphere, Atmos. Meas. Tech., 9, 4843–4859, https://doi.org/10.5194/amt-9-4843-2016, 2016.

Peters, G. P., Marland, G., Corinne Le Quéré, Boden, T., Canadell, J. G., and Raupach, M. R.: Rapid growth in co2 emissions after the 2008–2009 global financial crisis, Nat. Clim. Chang., 2, 2–4, https://doi.org/10.1038/nclimate1332, 2012.

Ran, L., Deng, Z., Wang, P., and Xia, X.: Black carbon and wavelength-dependent aerosol absorption in the North China Plain based on two-year aethalometer measurements, Atmos Environ., 142, 132 – 144, https://doi.org/10.1016/j.atmosenv.2016.07.014, 2016.

Ridder, T., Warneke, T., and Notholt, J.: Source brightness fluctuation correction of solar absorption fourier transform mid infrared spectra, Atmos. Meas. Tech., 4, 1045–1051, https://doi.org/10.5194/amt-4-1045-2011, 2011.

Robert, A. R. and Richard, A. M.: Air Pollution in China: mapping of concentrations and sources, PLoS One., 10, https://doi.org/10.1371/journal.pone.0135749, 2015.

Rodgers, C. D. and Connor, B. J.: Intercomparison of remote sounding instruments, J. Geophys. Res. Atmos., 108, https://doi.org/10.1029/2002JD002299, 2003.

Schneider, M., Hase, F., Blumenstock, T., Redondas, A., and Cuevas, E.: Quality assessment of O_3 profiles measured by a state-of-the-art ground-based FTIR observing system, Atmos. Chem. Phys., 8, 5579–5588, https://doi.org/10.5194/acp-8-5579-2008, 2008.

Song, Y. L., Achberger, C., and Linderholm, H. W.: Rain-season trends in precipitation and their effect in different climate regions of China during 1961–2008, Environ. Res. Lett., 6, 034 025, https://doi.org/10.1088/1748-9326/6/3/034025, 2011.

Toon, G., Blavier, J.-F., Washenfelder, R., Wunch, D., Keppel-Aleks, G., Wennberg, P., Connor, B., Sherlock, V., Griffith, D., Deutscher, N., and Notholt, J.: Total Column Carbon Observing Network (TCCON), OSA, https://doi.org/10.1364/FTS.2009.JMA3, 2009.

Toon, G. C.: Atmospheric Line List for the 2014 TCCON Data Release, https://doi.org/10.14291/tccon.ggg2014.atm.r0/1221656, 2017.

Toon, G. C. and Wunch, D.: A stand-alone a priori profile generation tool for GGG2014 release, https://doi.org/10.14291/tccon.ggg2014.priors.r0/1221661, 2015.

Velazco, V. A., Deutscher, N. M., Morino, I., Uchino, O., Bukosa, B., Ajiro, M., Kamei, A., Jones, N. B., C., P.-W., and Griffith, D. W. T.: Satellite and ground-based measurements of XCO$_2$ in a remote semiarid region of Australia, Earth Syst. Sci. Data, 11, 935–946, https://doi.org/10.5194/essd-11-935-2019, 2019.

Washenfelder, R. A., Toon, G. C., Blavier, J.-F., Yang, Z., Allen, N. T., Wennberg, P. O., Vay, S. A., Matross, D. M., and Daube, B. C.: Carbon dioxide column abundances at the Wisconsin Tall Tower site, J. Geophys. Res. Atmos., 111, https://doi.org/10.1029/2006JD007154, 2006.

Wennberg, P. O., Wunch, D., Roehl, C., Blavier, J.-F., Toon, G. C., and Allen, N.: TCCON data from Caltech (US), Release GGG2014R1, TCCON data archive, hosted by CaltechDATA, https://doi.org/10.14291/tccon.ggg2014.pasadena01.R1/1182415, https://tccondata.org, 2014.

Wennberg, P. O., Wunch, D., Roehl, C., Blavier, J.-F., Toon, G. C., Allen, N., Dowell, P., Teske, K., Martin, C., and Martin., J.: TCCON data from Lamont (US), Release GGG2014R1, TCCON data archive, hosted by CaltechDATA, https://doi.org/10.14291/tccon.ggg2014.lamont01.R1/1255070, https://tccondata.org, 2016.

WMO: WMO Greenhouse Gas Bullitin, 14, https://library.wmo.int/index.php?lvl=notice_display&id=20697#.XcMDaONpxGQ, 2018.

Wunch, D., Toon, G. C., Wennberg, P. O., Wofsy, S. C., Stephens, B. B., Fischer, M. L., Uchino, O., Abshire, J. B., Bernath, P., Biraud, S. C., Blavier, J.-F. L., Boone, C., Bowman, K. P., Browell, E. V., Campos, T., Connor, B. J., Daube, B. C., Deutscher, N. M., Diao, M., Elkins, J. W., Gerbig, C., Gottlieb, E., Griffith, D. W. T., Hurst, D. F., Jiménez, R., Keppel-Aleks, G., Kort, E. A., Macatangay, R., Machida, T., Matsueda, H., Moore, F., Morino, I., Park, S., Robinson, J., Roehl, C. M., Sawa, Y., Sherlock, V., Sweeney, C., Tanaka, T., and Zondlo, M. A.: Calibration of the Total Carbon Column Observing Network using aircraft profile data, Atmos. Meas. Tech., 3, 1351–1362, https://doi.org/10.5194/amt-3-1351-2010, 2010.

Wunch, D., Toon, G. C., Blavier, J.-F. L., Washenfelder, R. A., Notholt, J., Connor, B. J., Griffith, D. W. T., Sherlock, V., and Wennberg, P. O.: The Total Carbon Column Observing Network, Philos. Trans. Royal Soc. A., 369, 2087–2112, https://doi.org/10.1098/rsta.2010.0240, 2011a.

Wunch, D., Wennberg, P. O., Toon, G. C., Connor, B. J., Fisher, B., Osterman, G. B., Frankenberg, C., Mandrake, L., O'Dell, C., Ahonen, P., Biraud, S. C., Castano, R., Cressie, N., Crisp, D., Deutscher, N. M., Eldering, A., Fisher, M. L., Griffith, D. W. T., Gunson, M., Heikkinen, P., Keppel-Aleks, G., Kyrö, E., and et al.: A method for evaluating bias in global measurements of CO$_2$ total columns from space, Atmos. Chem. Phys., 11, 12 317–12 337, https://doi.org/10.5194/acp-11-12317-2011, 2011b.

Wunch, D., Toon, G. C., Sherlock, V., Deutscher, N. M., Liu, C., Feist, D. G., and Wennberg, P. O.: Documentation for the 2014 TCCON Data Release, https://doi.org/10.14291/tccon.ggg2014.documentation.r0/1221662, https://data.caltech.edu/records/249, 2015.

Wunch, D., Wennberg, P. O., Osterman, G., Fisher, B., Naylor, B., Roehl, C. M., O'Dell, C., Mandrake, L., Viatte, C., Kiel, M., Griffith, D. W. T., Deutscher, N. M., Velazco, V. A., Notholt, J., Warneke, T., Petri, C., De Maziere, M., Sha, M. K., Sussmann, R., Rettinger, M., Pollard, D., Robinson, J., Morino, I., Uchino, O., Hase, F., Blumenstock, T., Feist, D. G., Arnold, S. G., Strong, K., Mendonca, J., Kivi, R., Heikkinen, P., Iraci, L., Podolske, J., Hillyard, P. W., Kawakami, S., Dubey, M. K., Parker, H. A., Sepulveda, E., García, O. E., Te, Y., Jeseck, P., Gunson, M. R., Crisp, D., and Eldering, A.: Comparisons of the Orbiting Carbon Observatory-2 (OCO-2) X_{CO_2} measurements with TCCON, Atmos. Meas. Tech., 10, 2209–2238, https://doi.org/10.5194/amt-10-2209-2017, 2017.

Yang, Y., Zhou, M., Langerock, B., Sha, M., Hermans, C., Wang, T., Ji, D., Vigouroux, C., Kumps, N., Wang, G., De Mazière, M., and Wang, P.: Ground-based FTIR CO$_2$, CH$_4$ and CO measurements at Xianghe, China, https://doi.org/10.18758/71021049, 2019.

Yin, Y., Chevallier, F., Ciais, P., Broquet, G., Fortems-Cheiney, A., Pison, I., and Saunois, M.: Decadal trends in global CO emissions as seen by MOPITT, Atmos. Chem. Phys., 15, 13 433–13 451, https://doi.org/10.5194/acp-15-13433-2015, 2015.

Zheng, B., Frederic, C., Philippe, C., Y., Y., D., M. N., W., H. M., W., Y., Z., Q., and H., K.: Rapid decline in carbon monoxide emissions and export from East Asia between years 2005 and 2016, Environ. Res. Lett., 13, 044 007, https://doi.org/10.1088/1748-9326/aab2b3, 2018.

5 Zhou, M., Dils, B., Wang, P., Detmers, R., Yoshida, Y., O'Dell, C. W., Feist, D. G., Velazco, V. A., Schneider, M., and De Mazière, M.: Validation of TANSO-FTS/GOSAT XCO_2 and XCH_4 glint mode retrievals using TCCON data from near-ocean sites, Atmos. Meas. Tech., 9, 1415–1430, https://doi.org/10.5194/amt-9-1415-2016, 2016.
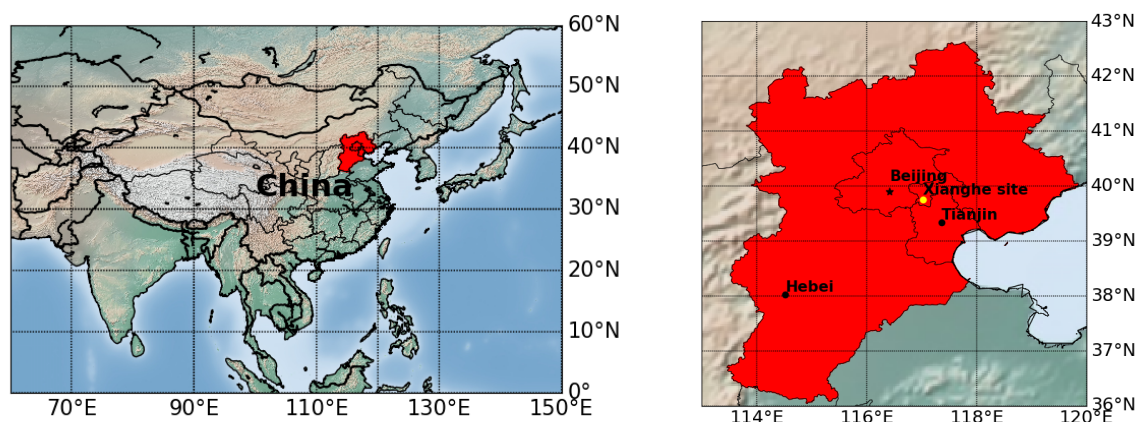
Figure 1. Map of China, the Beijing-Tianjin-Hebei region is the red shadow area which is also zoomed in the right panel. It is one of the most populous and economically dynamic regions in China. Xianghe site (yellow spot in the right panel) is located in Xianghe county, about 50km to the east-southeast of Beijing and 70 km to the north-northwest of Tianjin, acting an integrated transportation and transfer center in this region.
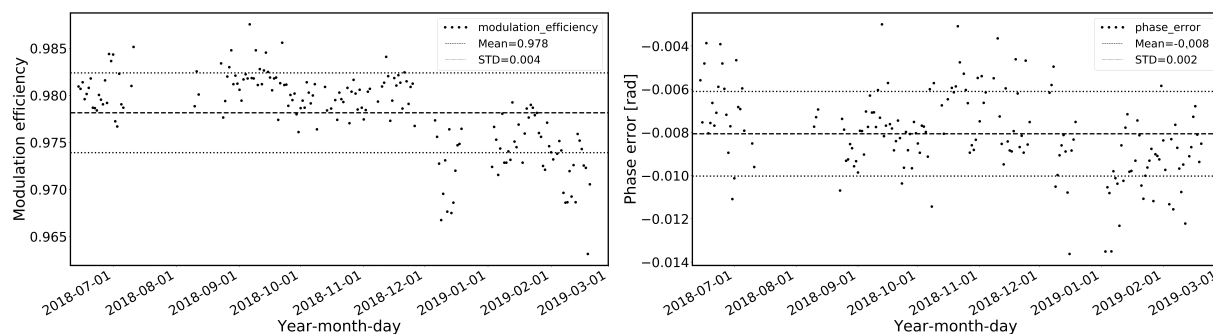
Figure 2. The time series of retrieved modulation efficiency (left panel) and phase error (right panel) at maximum optical path difference (45cm).
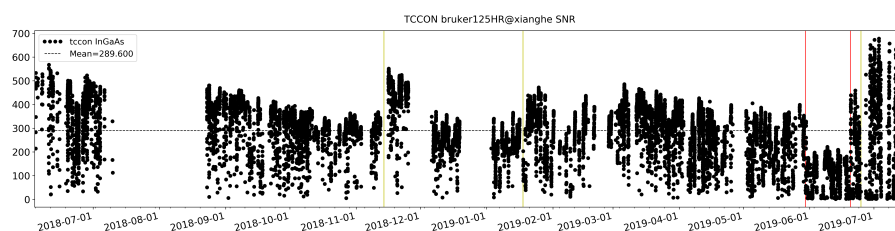
Figure 3. Time series of the signal-to-noise ratio (SNR) of the InGaAs spectra from the FTIR in Xianghe. The yellow lines indicate solar tracker maintenances: cleaning of the mirrors on 14 November 2018 and 25 June 2019, and replacement of the degraded mirror on February 1, 2019. The first red line indicates the day when we add DC signal recording (31 May 2019) and the second red line indicates the day when the aperture was increased from 0.5mm to 0.8mm (19 June 2019).
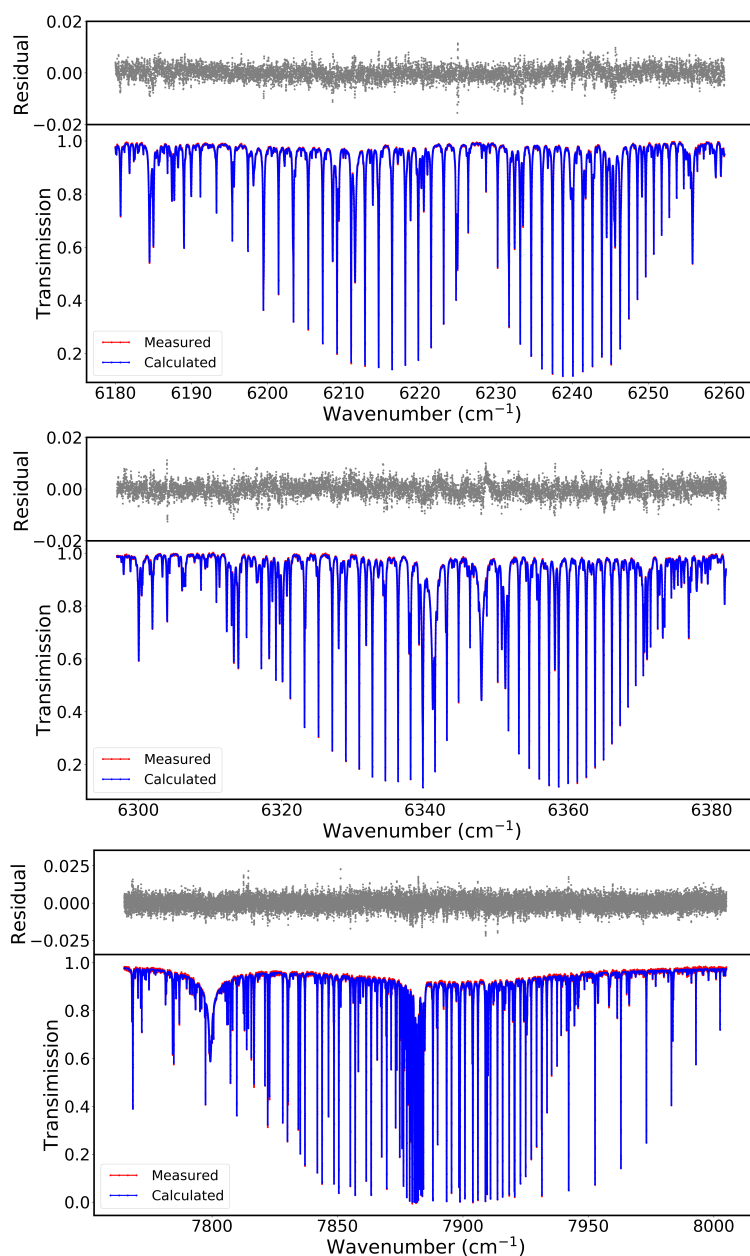
Figure 4. Measured and calculated spectrum of CO_2 in spectral window of 6180-6260 cm^{-1} (upper panel), CO_2 in spectral window of 6297-6382 cm^{-1} (middle panel) and O_2 in spectral window of 7765-8005 cm^{-1} (bottom panel).
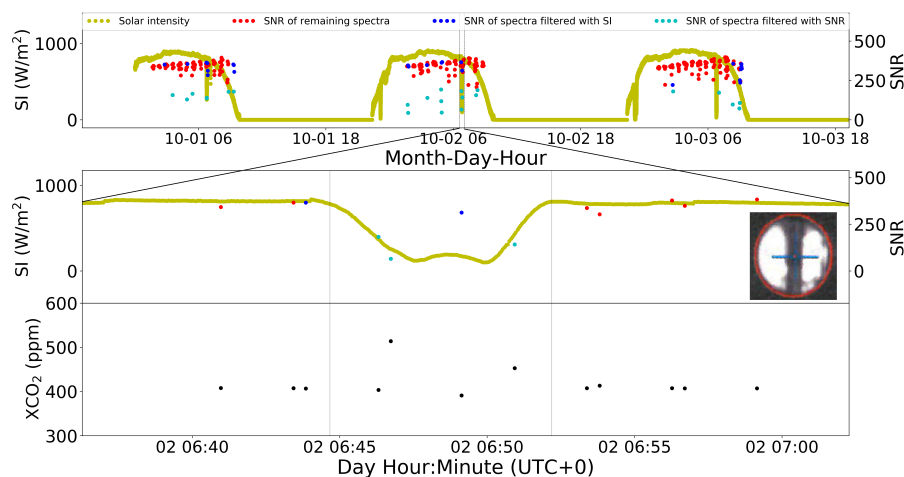
Figure 5. The solar direct intensity from 1 October 2018 to 3 October 2018, with a zoom on the time period between 6:36 and 7:02 (UTC) on 2 October 2018 when the tower shadow is observed by the FTIR (see the inside camera image, middle panel). The blue dots in the upper panel denote the SNR of spectra filtered with solar intensity (SI), the cyan dots denote the SNR of spectra filtered with SNR, and the red dots denote the SNR of spectra after both filtering. The affected XCO_2 retrieval during the shadow appearing time are displayed in the bottom panel.
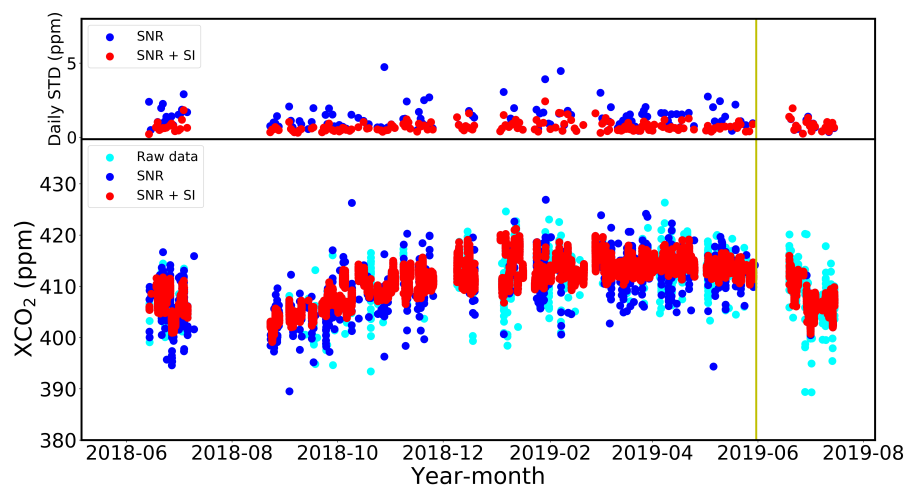
Figure 6. Time series of XCO_2 from 14 June 2018 to 19 July 2019 before and after spectra selection. The cyan dots denote all the raw data, the blue dots in bottom panel are those retrieved XCO_2 after SNR filtering and the red dots are those retrieved XCO_2 after SNR + SI filtering. In upper panel, the blue dots denote the daily standard deviation of XCO_2 only with SNR filtering while the red ones denote those with SNR + SI filtering. The yellow line denotes the day (31 May 2019) when we added the DC signal recording.
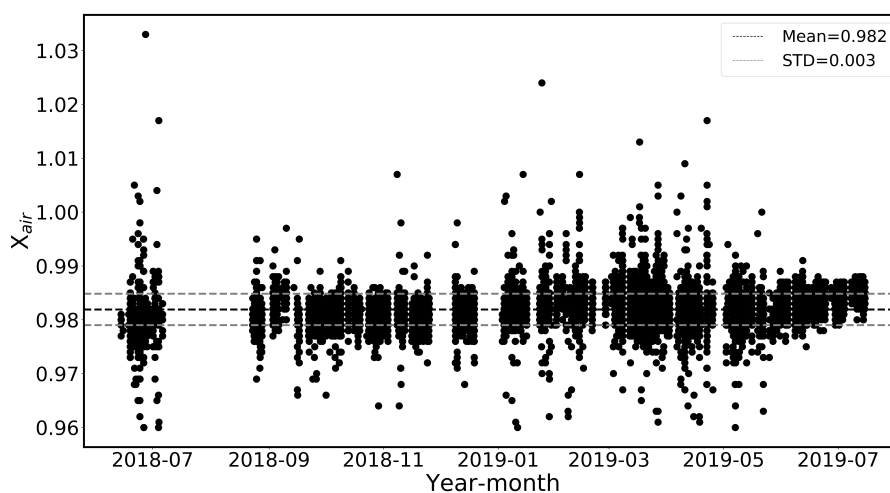
Figure 7. Time series of X_{air}.
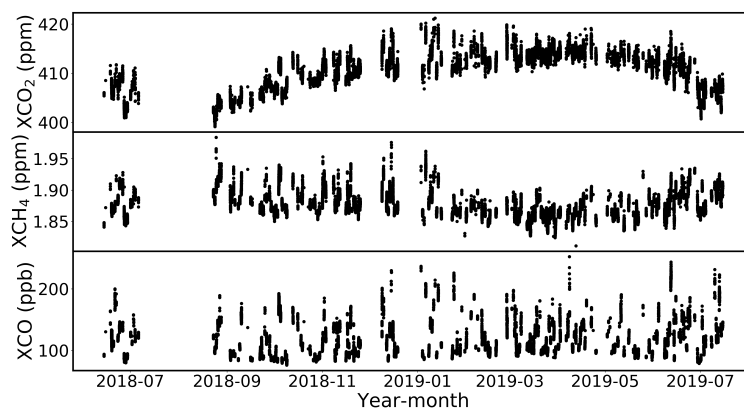
Figure 8. Time series of XCO_2, XCH_4 and XCO covering the period from 14 June 2018 to 19 July 2019.
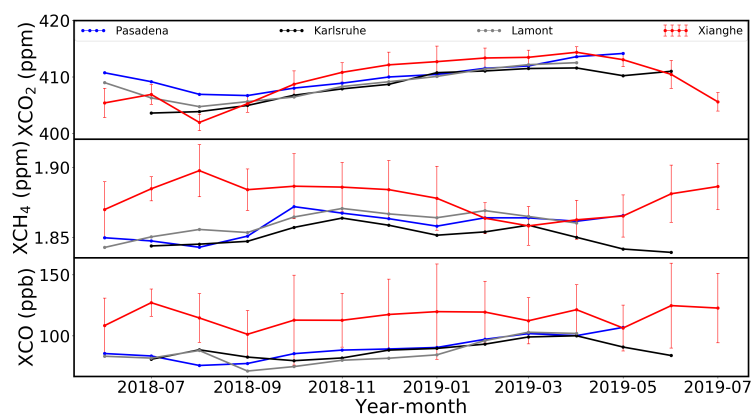
Figure 9. Monthly mean of XCO_2, XCH_4 and XCO at Pasadena, Karlsruhe, Lamont and Xianghe. The error bars are the monthly STDs of XCO_2, XCH_4 and XCO at Xianghe.
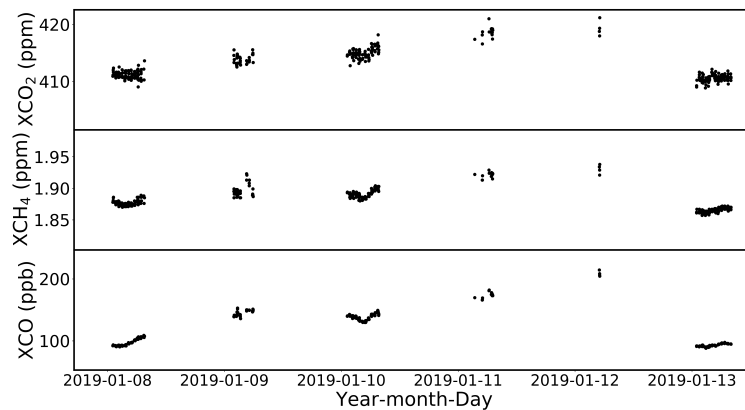
Figure 10. The day-to-day variations from 8 January to 13 January 2019 for XCO_2, XCH_4 and XCO at Xianghe.
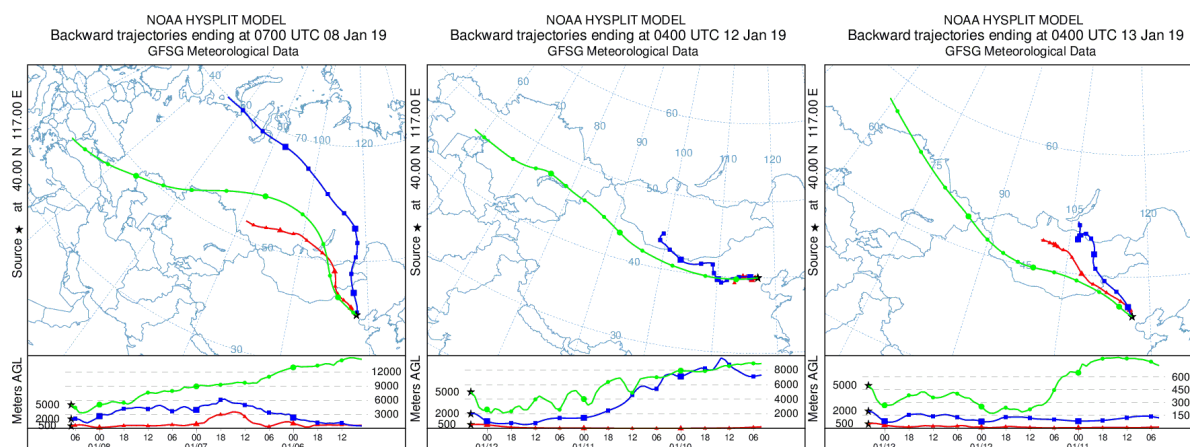
Figure 11. Back trajectories of 72 h at Xianghe were calculated using NOAA HYSPLIT. Trajectories arrive at altitudes of 500m, 2000m and 5000m above ground level at each local noon on 8 January 2019 (left panel), 12 January 2019 (middle panel) and 13 January 2019 (right panel).
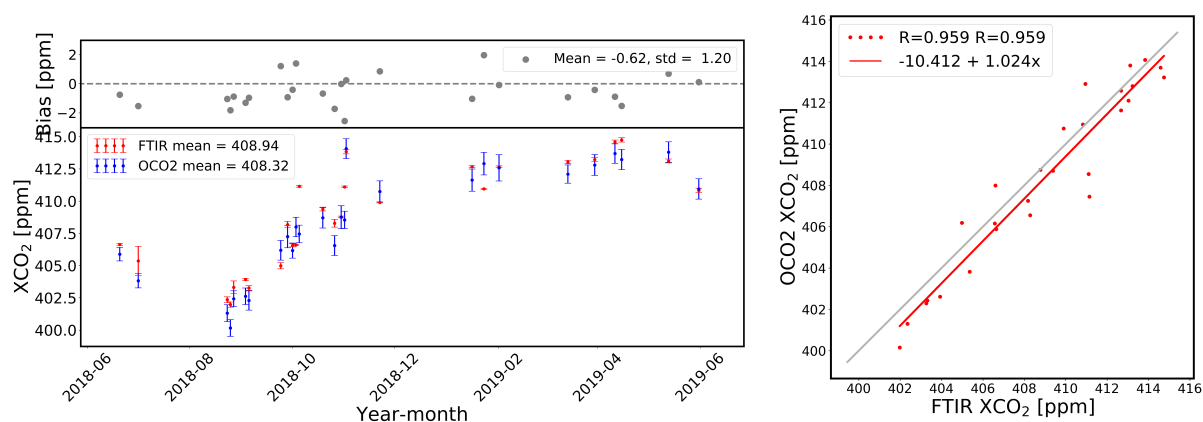
Figure 12. Left panel: Time series of daily mean collocated OCO-2 and ground-based FTIR XCO$_2$ data at Xianghe (lower plot) and the bias between them (upper plot). Right panel: Correlation plot between collocated daily mean XCO$_2$ data from OCO-2 and FTIR at Xianghe.
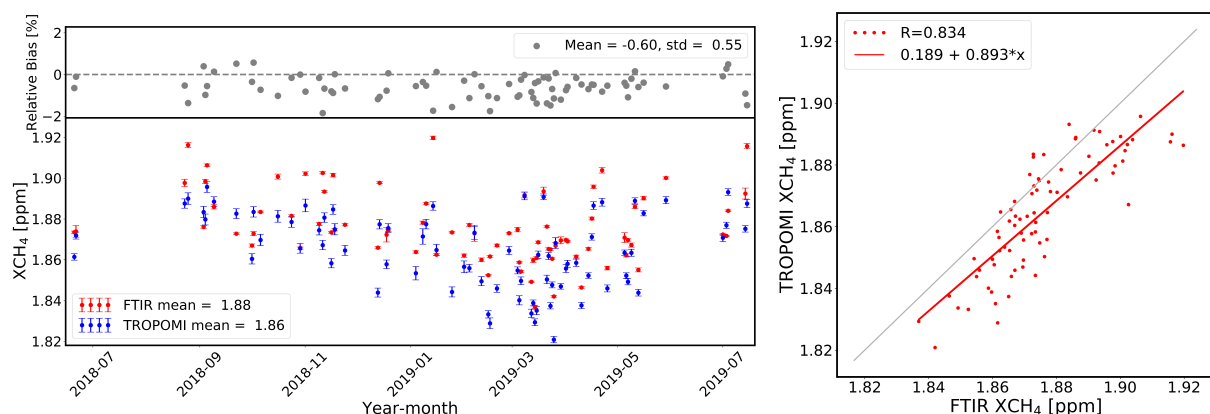
Figure 13. Left panel: Time series of daily mean collocated TROPOMI and ground-based FTIR XCH₄ data at Xianghe (lower plot) and the bias between them (upper plot). Right panel: Correlation plot between collocated daily mean XCH₄ data from TROPOMI and FTIR at Xianghe.
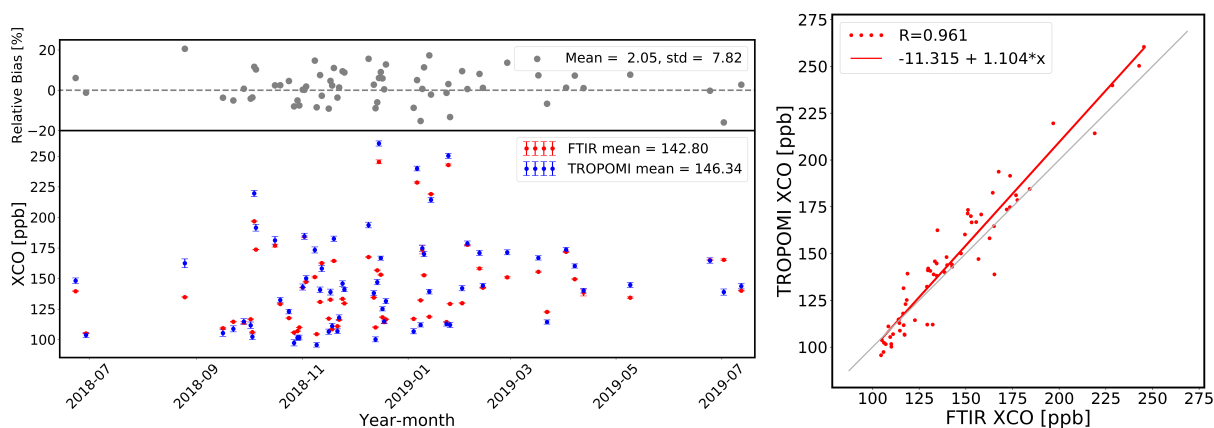
Figure 14. Left panel: Time series of daily mean collocated TROPOMI and ground-based FTIR XCO data at Xianghe (lower plot) and the bias between them (upper plot). Right panel: Correlation plot between collocated daily mean XCO data from TROPOMI and FTIR at Xianghe.

Table 1. The standard deviation (STD) of XCO_2, XCH_4 and XCO of the remaining data after each solar intensity (SI) filtering and the percentage of the remaining spectra number from 14 June 2018 to 31 December 2018.

β	γ	STD(XCO_2)	STD(XCH_4)	STD(XCO)	Percentage of remaining spectra
(%)	(%)	(ppm)	(ppm)	(ppb)	(%)
85	10	0.918	0.0066	5.525	89.5
85	5	0.889	0.0065	5.516	88.9
85	0	0.881	0.0064	5.512	88.1
90	10	0.782	0.0062	5.423	86.6
90	5	0.772	0.0061	5.391	85.8
90	0	0.732	0.0061	5.298	84.7
95	10	0.682	0.0059	5.299	78.5
95	5	0.680	0.0058	5.233	77.1
95	0	0.670	0.0058	5.206	75.2

Table 2. Average XCO_2 daily standard deviation after (a) no filtering, (b) SNR filtering, (c) both SNR filtering and SI filtering during the AC mode and AC+DC mode periods. The unit is ppm.

	AC mode	AC+DC mode
a	1.39	1.34
b	1.14	0.76
c	0.71	0.83